Biomedical Optics EXPRESS

Rapid monitoring of cerebral ischemia dynamics using laser-based optical imaging of blood oxygenation and flow

Hart Levy,[1,2] Dene Ringuette,[1] and Ofer Levi[1,2,*]

[1]*Institute of Biomaterials and Biomedical Engineering, University of Toronto, 164 College Street, Toronto, Ontario, M5S 3G9,Canada*

[2]*The Edward S. Rogers Sr. Department of Electrical and Computer Engineering, University of Toronto, 10 King's College Road, Toronto, Ontario, M5S 3G4, Canada*

**ofer.levi@utoronto.ca*

Abstract: Imaging blood flow or oxygenation changes using optical techniques is useful for monitoring cortical activity in healthy subjects as well as in diseased states such as stroke or epilepsy. However, in order to gain a better understanding of hemodynamics in conscious, freely moving animals, these techniques must be implemented in a small scale, portable design that is adaptable to a wearable format. We demonstrate a novel system which combines the two techniques of laser speckle contrast imaging and intrinsic optical signal imaging simultaneously, using compact laser sources, to monitor induced cortical ischemia in a full field format with high temporal acquisition rates. We further demonstrate the advantages of using combined measurements of speckle contrast and oxygenation to establish absolute flow velocities, as well as to statistically distinguish between veins and arteries. We accomplish this system using coherence reduction techniques applied to Vertical Cavity Surface Emitting Lasers (VCSELs) operating at 680, 795 and 850 nm. This system uses minimal optical components and can easily be adapted into a portable format for continuous monitoring of cortical hemodynamics.

OCIS codes: (170.0110) Imaging systems; (170.3880) Medical and biological imaging; (140.2020) Diode lasers; (170.6480) Spectroscopy, speckle.

References and links

1. A. Devor, I. Ulbert, A. K. Dunn, S. N. Narayanan, S. R. Jones, M. L. Andermann, D. A. Boas, and A. M. Dale, "Coupling of the cortical hemodynamic response to cortical and thalamic neuronal activity," Proc. Natl. Acad. Sci. U.S.A. **102**(10), 3822–3827 (2005).
2. P. B. Jones, H. K. Shin, D. A. Boas, B. T. Hyman, M. A. Moskowitz, C. Ayata, and A. K. Dunn, "Simultaneous multispectral reflectance imaging and laser speckle flowmetry of cerebral blood flow and oxygen metabolism in focal cerebral ischemia," J. Biomed. Opt. **13**(4), 044007 (2008).
3. F. Di Salle, E. Formisano, D. E. Linden, R. Goebel, S. Bonavita, A. Pepino, F. Smaltino, and G. Tedeschi, "Exploring brain function with magnetic resonance imaging," Eur. J. Radiol. **30**(2), 84–94 (1999).
4. T. H. Schwartz, S.-B. Hong, A. P. Bagshaw, P. Chauvel, and C.-G. Bénar, "Preictal changes in cerebral haemodynamics: review of findings and insights from intracerebral EEG," Epilepsy Res. **97**(3), 252–266 (2011).
5. A. K. Dunn, H. Bolay, M. A. Moskowitz, and D. A. Boas, "Dynamic imaging of cerebral blood flow using laser speckle," J. Cereb. Blood Flow Metab. **21**(3), 195–201 (2001).
6. J. C. Eliassen, E. L. Boespflug, M. Lamy, J. Allendorfer, W. J. Chu, and J. P. Szaflarski, "Brain-mapping techniques for evaluating poststroke recovery and rehabilitation: a review," Top. Stroke Rehabil. **15**(5), 427–450 (2008).
7. K. Masamoto, T. Kim, M. Fukuda, P. Wang, and S. G. Kim, "Relationship between neural, vascular, and BOLD signals in isoflurane-anesthetized rat somatosensory cortex," Cereb. Cortex **17**(4), 942–950 (2007).
8. B. A. Flusberg, E. D. Cocker, W. Piyawattanametha, J. C. Jung, E. L. Cheung, and M. J. Schnitzer, "Fiber-optic fluorescence imaging," Nat. Methods **2**(12), 941–950 (2005).
9. P. Miao, H. Y. Lu, Q. Liu, Y. Li, and S. B. Tong, "Laser speckle contrast imaging of cerebral blood flow in freely moving animals," J. Biomed. Opt. **16**(9), 090502 (2011).

#160425 - $15.00 USD Received 22 Dec 2011; revised 10 Feb 2012; accepted 26 Mar 2012; published 27 Mar 2012

10. K. K. Ghosh, L. D. Burns, E. D. Cocker, A. Nimmerjahn, Y. Ziv, A. E. Gamal, and M. J. Schnitzer, "Miniaturized integration of a fluorescence microscope," Nat. Methods **8**(10), 871–878 (2011).
11. M. B. Bouchard, B. R. Chen, S. A. Burgess, and E. M. Hillman, "Ultra-fast multispectral optical imaging of cortical oxygenation, blood flow, and intracellular calcium dynamics," Opt. Express **17**(18), 15670–15678 (2009).
12. A. J. Foust, J. L. Schei, M. J. Rojas, and D. M. Rector, "In vitro and in vivo noise analysis for optical neural recording," J. Biomed. Opt. **13**(4), 044038 (2008).
13. A. K. Dunn, A. Devor, H. Bolay, M. L. Andermann, M. A. Moskowitz, A. M. Dale, and D. A. Boas, "Simultaneous imaging of total cerebral hemoglobin concentration, oxygenation, and blood flow during functional activation," Opt. Lett. **28**(1), 28–30 (2003).
14. Z. Luo, Z. Yuan, Y. Pan, and C. Du, "Simultaneous imaging of cortical hemodynamics and blood oxygenation change during cerebral ischemia using dual-wavelength laser speckle contrast imaging," Opt. Lett. **34**(9), 1480–1482 (2009).
15. E. A. Munro, H. Levy, D. Ringuette, T. D. O'Sullivan, and O. Levi, "Multi-modality optical neural imaging using coherence control of VCSELs," Opt. Express **19**(11), 10747–10761 (2011).
16. R. Michalzik and K. J. Ebeling, "Operating Principles of VCSELs," in *Vertical-Cavity Surface-Emitting Laser Devices*, H. Li, and K. Iga, eds. (Springer-Verlag, Berlin, 2003), pp. 53–98.
17. J. W. Goodman, "Some fundamental properties of speckle," J. Opt. Soc. Am. **66**(11), 1145–1150 (1976).
18. B. E. A. Saleh and M. C. Teich, *Fundamentals of Photonics* (Wiley, Hoboken, NJ, 2007).
19. F. Adhami, G. Liao, Y. M. Morozov, A. Schloemer, V. J. Schmithorst, J. N. Lorenz, R. S. Dunn, C. V. Vorhees, M. Wills-Karp, J. L. Degen, R. J. Davis, N. Mizushima, P. Rakic, B. J. Dardzinski, S. K. Holland, F. R. Sharp, and C. Y. Kuan, "Cerebral ischemia-hypoxia induces intravascular coagulation and autophagy," Am. J. Pathol. **169**(2), 566–583 (2006).
20. W. J. Tom, A. Ponticorvo, and A. K. Dunn, "Efficient processing of laser speckle contrast images," IEEE Trans. Med. Imaging **27**(12), 1728–1738 (2008).
21. C. H. Chen-Bee, T. Agoncillo, Y. Xiong, and R. D. Frostig, "The triphasic intrinsic signal: implications for functional imaging," J. Neurosci. **27**(17), 4572–4586 (2007).
22. A. J. Blood and A. W. Toga, "Optical intrinsic signal imaging responses are modulated in rodent somatosensory cortex during simultaneous whisker and forelimb stimulation," J. Cereb. Blood Flow Metab. **18**(9), 968–977 (1998).
23. O. Yang, D. Cuccia, and B. Choi, "Real-time blood flow visualization using the graphics processing unit," J. Biomed. Opt. **16**(1), 016009–016014 (2011).
24. J. C. Ramirez-San-Juan, R. Ramos-García, I. Guizar-Iturbide, G. Martínez-Niconoff, and B. Choi, "Impact of velocity distribution assumption on simplified laser speckle imaging equation," Opt. Express **16**(5), 3197–3203 (2008).
25. J. C. Ramírez-San-Juan, Y. C. Huang, N. Salazar-Hermenegildo, R. Ramos-García, J. Muñoz-Lopez, and B. Choi, "Integration of image exposure time into a modified laser speckle imaging method," Phys. Med. Biol. **55**(22), 6857–6866 (2010).
26. H. F. Zhang, K. Maslov, M. Sivaramakrishnan, G. Stoica, and L. V. Wang, "Imaging of hemoglobin oxygen saturation variations in single vessels in vivo using photoacoustic microscopy," Appl. Phys. Lett. **90**(5), 053901 (2007).
27. R. Hebel and M. W. Stromberg, *Anatomy and Embryology of the Laboratory Rat* (BioMed Verlag, 1986).
28. H. K. Shin, A. K. Dunn, P. B. Jones, D. A. Boas, M. A. Moskowitz, and C. Ayata, "Vasoconstrictive neurovascular coupling during focal ischemic depolarizations," J. Cereb. Blood Flow Metab. **26**(8), 1018–1030 (2006).
29. K. A. Hossmann, "Periinfarct depolarizations," Cerebrovasc. Brain Metab. Rev. **8**(3), 195–208 (1996).
30. D. A. Boas and A. K. Dunn, "Laser speckle contrast imaging in biomedical optics," J. Biomed. Opt. **15**(1), 011109 (2010).
31. M. R. Zhao, J. Nguyen, H. T. Ma, N. Nishimura, C. B. Schaffer, and T. H. Schwartz, "Preictal and ictal neurovascular and metabolic coupling surrounding a seizure focus," J. Neurosci. **31**(37), 13292–13300 (2011).
32. T. H. Schwartz, "Neurovascular coupling and epilepsy: hemodynamic markers for localizing and predicting seizure onset," Epilepsy Curr. **7**(4), 91–94 (2007).
33. P. Padmawar, X. Yao, O. Bloch, G. T. Manley, and A. S. Verkman, "K+ waves in brain cortex visualized using a long-wavelength K+-sensing fluorescent indicator," Nat. Methods **2**(11), 825–827 (2005).
34. F. Amzica, M. Massimini, and A. Manfridi, "Spatial buffering during slow and paroxysmal sleep oscillations in cortical networks of glial cells in vivo," J. Neurosci. **22**(3), 1042–1053 (2002).
35. S. Dufour, P. Dufour, O. Chever, R. Vallée, and F. Amzica, "In vivo simultaneous intra- and extracellular potassium recordings using a micro-optrode," J. Neurosci. Methods **194**(2), 206–217 (2011).

1. Introduction

In the quantification of neural signals in healthy and diseased states, hemodynamic measurements have proven very valuable, giving signals which are well correlated with data collected from electrophysiology measurements [1]. The use of optical techniques for

#160425 - $15.00 USD Received 22 Dec 2011; revised 10 Feb 2012; accepted 26 Mar 2012; published 27 Mar 2012

producing wide field maps of hemodynamic properties such as blood oxygenation and blood flow speeds has become an increasingly prevalent option in the neuroimaging community. In particular, Intrinsic Optical Signal Imaging (IOSI) and Laser Speckle Contrast Imaging (LSCI) are often used, respectively, as complementary methods for quantifying blood oxygenation and flow speeds [2]. The ability to obtain high spatial and temporal resolution data with inexpensive equipment has made optical imaging a desirable alternative to commonly used clinical techniques such as fMRI, SPECT or PET. Furthermore, the option of using optical techniques to simultaneously quantify both oxygenation and flow rates allows researchers to gain further insight into the nature of hemodynamic response and neurovascular coupling. This provides an added dimension beyond the data typically obtained using fMRI, which generally cannot distinguish clearly between the effects of oxygen metabolization and compensatory flow [3]. In many disease scenarios, such as stroke or epilepsy, this distinction is important in providing a thorough understanding of the mechanism of dysfunction. In epilepsy, for example, there remain questions involving increases of cerebral blow flow seen prior to ictal events, and whether this increase is sufficient to supply increased metabolic demand [4]. In stroke, understanding flow as well as oxygenation changes is a key factor in determining the extent of the ischemic core and of the penumbra [5]. Monitoring hemodynamics effectively after an ischemic event can also be used as a metric for measuring and understanding stroke recovery [6].

In many cases, animal models can provide insight into diseased states as they would apply to humans. However, the restrictions associated with many imaging studies limit their applicability to more realistic scenarios; due to high sensitivity to any movement, general anesthesia is almost always used. The effects of anesthesia on hemodynamic responses limit the neural signals that can be imaged [7]. As a result, portable and real time imaging techniques have become increasingly desirable to allow imaging of fully conscious, active animals participating in normal behaviors.

Several attempts have been made to implement portable optical imaging techniques, with some success. Portable two-photon imaging techniques have been used to provide high resolution images of flow and anatomy but suffer from the same difficulties found in large scale two-photon imaging [8]. A high-cost tabletop laser is needed to produce illumination and requires alignment between imaging sessions. Further, costly dyes are needed to produce the required two-photon fluorescence signal. With the use of fiber bundles to illuminate and collect fluorescent emission, very high-resolution images can be produced, but the field of view is limited and light collection efficiency is significantly reduced. For these reasons, fully integrated, wide-field imaging techniques are preferable in portable imaging. Several other portable systems that produce full-field imaging using modalities such as LSCI or fluorescence have been recently introduced. These scaled down imaging solutions are made feasible with small-scale CMOS imagers and compact illumination, or using tethered fiber optics to bring illumination to and from an animal [9,10], but are limited to single modality applications. The inclusion and control of multiple illumination sources and optical components needed for multiple imaging techniques, operated simultaneously, leads to further complexities in the development of portable sensors. In order to diversify the data obtained with portable imaging formats, further steps are needed to integrate multiple techniques simultaneously. The data garnered from combined imaging of blood flow, oxygenation and fluorescence can be applied to develop a better understanding of real time hemodynamics and other physiological changes. This provides a more complete picture of the numerous processes occurring along with neural activity in diseased and healthy states [11].

1.1. Simultaneous IOSI and LSCI with VCSELs

In many applications, it is difficult to apply LSCI and IOSI in tandem due to disparities between the illumination sources required. While LSCI requires a highly coherent laser source to produce the speckle needed to discern flow, IOSI makes use of a low coherence, wider

#160425 - $15.00 USD Received 22 Dec 2011; revised 10 Feb 2012; accepted 26 Mar 2012; published 27 Mar 2012

spectrum source to produce the low noise illumination needed to measure small fluctuations in reflectance [12]. Several systems have been developed using separate light sources or cameras to apply both techniques simultaneously; none are adaptable to a portable format [2,13,14]. Techniques that image oxygenation with an incoherent source, such as an LED, cannot provide the speckle necessary for LSCI. However, low noise sources can be used in a 'line scan' spatiotemporal correlation technique to track individual cell motion in vessels and directly quantify speeds [11]. The difficulties with this 'line scan' technique include that it is computationally intensive, requires very high frame rates, and can generally only be completed on a small region at a time. To solve this problem, we have developed a system that uses coherence control of Vertical Cavity Surface Emitting Lasers (VCSELs) to produce illumination satisfying the needs of both IOSI and LSCI from a single source in a specialized current sweep (SW) operation scheme. When operated near threshold, these devices are able to produce highly coherent single mode (SM) laser illumination. In contrast, by taking advantage of thermal effects within the small laser cavity, application of rapidly modulated current (the SW operation scheme) broadens the effective spectrum of a VCSEL, leading to reduced coherence [15]. This property is particular to VCSELs as their small gain volume allows rapid thermal changes to produce spectral effects on a very short time scale [16].

Using VCSELs as a source for both LSCI and IOSI offers some advantages over setups which may include multiple source types. Combined devices which use both micro-LED components and laser diodes could provide the required illumination, but lack several properties which make VCSELs better suited for portable imaging. Power consumption is one important constraint when developing a portable device. Micro LED packages may be able to provide slightly stronger illumination than VCSELs, but at greatly reduced efficiency. An LED may produce 5-10 mW output power with 200 mW input. VCSELs, on the other hand, can easily provide 2-5 mW output with only 10-20 mW input. Use of LEDs for IOSI inherently leads to another constraint, due to their associated broad spectra. If one wishes to use LEDs for spectroscopic applications, a notch filter is generally required to narrow down the illumination spectrum if accurate results are desired. Large scale optical elements are not amenable to portable imaging scenarios, and incorporating micro filters at each wavelength used would lead to greatly increased cost.

VCSELs offer further advantages over many other laser sources in scenarios with rapid on/off cycles. Due to their narrow gain region, VCSELs can reach thermal stability within microseconds following the application of a current. Edge emitting lasers often require several minutes of warm-up time, before both wavelength and power stability is achieved. By using VCSELs for both IOSI and LSCI, stability is ensured and the lasers can be rapidly pulsed in each operation mode.

The theoretical basis of laser speckle has been widely developed. Studies have pointed to several avenues to reduce the speckle contrast intensity observed from a given source [17]. The main methods used are polarization diversity, angle diversity, and wavelength diversity. In each case, if we view the source as providing n_s superimposed speckle patterns, distinguishable based on a particular separation criterion, speckle contrast will be reduced by the square root of n_s. For the purpose of tissue imaging, we focus on wavelength diversity. When illuminating a rough surface, the wavelength separation criterion is derived from the standard deviation of the surface level [17]:

$$\delta\lambda = \frac{\lambda_c^{\,2}}{2\sigma_s} \tag{1}$$

$\delta\lambda$ is the wavelength separation needed to consider two patterns to be distinct, σ_s is the surface deviation, and λ_c is the central wavelength of illumination. If instead, a broad spectrum source with width $\Delta\lambda = n_s\delta\lambda$ is used, then n_s distinct patterns will be present. We can write a new relation for the number of distinct patterns as follows:

#160425 - $15.00 USD Received 22 Dec 2011; revised 10 Feb 2012; accepted 26 Mar 2012; published 27 Mar 2012

$$n_s = \frac{2\sigma_s}{\lambda_c^{\,2} / \Delta\lambda} \tag{2}$$

We can relate this expression to an illumination source's temporal coherence, by identifying a common equation which is used to estimate the coherence length, l_c, using the full width half max (FWHM) spectral width [18]:

$$l_c = \frac{2\ln 2}{\pi}\frac{\lambda_c^{\,2}}{\Delta\lambda} \tag{3}$$

This relation only applies to a Gaussian spectral profile but can be used as an estimate in other cases. By including this relation we can arrive at an expression directly relating the surface roughness σ_s and coherence length l_c to contrast reduction by $\sqrt{n_s}$:

$$n_s = \frac{4\ln 2\sigma_s}{\pi l_c} \approx \frac{\sigma_s}{l_c} \tag{4}$$

Finally, when imaging tissue the surface roughness becomes difficult to define, as the optical paths are dominated by scattering within the tissue. In this case, the standard deviation of optical path lengths in tissue may be used instead. This quantity is best modeled using Monte Carlo simulation. It is this effect of averaging superimposed speckles which allows reduction of speckle noise using SW operation spectral broadening in VCSELs. By reducing coherence length, we increase n_s as seen in tissue, which leads to a related decrease in speckle contrast. In this study, we demonstrate an implementation of multi-wavelength IOSI and LSCI which takes advantage of this effect, using current swept VCSELs at 680, 795, 850 nm. The combined technique is easily modifiable to a portable format, allowing for real time imaging of conscious, freely moving animals.

2. Materials and methods

2.1. Device characterization

VCSEL devices of three wavelengths were characterized using an optical spectrum analyzer (OSA, Ando AQ6317B) and using interferometry. The devices' spectra were measured with SM (at threshold current), MM (at peak power), and optimized SW (current sweep) operation schemes. SW spectral widths were used to predict coherence lengths using Eq. (3). For verification of the reduced coherence, a Michelson interferometer was used to measure the coherence lengths of each device under SW operation. The resulting data were used to estimate the expected contrast reduction in tissue.

VCSEL spectra are shown in Fig. 1(a). Wavelengths were selected based on available VCSEL technologies, and matched to 3 regions of the Hb spectra which provide important signals for IOSI. 680 nm is near a minimum of HbO absorption, and reflects mostly changes in HbR. 795 nm is near an isobestic point of the spectra, and reflects total Hb changes. 850 nm is near a minimum for HbR absorption, and reflects mostly HbO changes. The MM operation currents were determined based on the maximum power levels of each wavelength, while SW operation currents covered the range from threshold to somewhat above peak power. Spectra in the SM case are seen to be narrower than 0.04 nm, and the results shown here are most likely limited by OSA resolution rather than the spectra themselves. For MM operation, a wavelength shift can be seen, as well as the appearance of higher order side bands. For each wavelength, a similar effect is seen in the application of SW operation. The spectra are broadened to a width in the range of 2 nm, spanning the full range of available wavelengths.

Interferogram results for the three wavelengths' SW operation are shown in Fig. 1(b). Similar results are seen in all three cases and coherence lengths are found to be in the range of 90-230 μm. If we use Monte Carlo simulated values of σ_s in Eq. (4), we can estimate n_s to be

#160425 - $15.00 USD Received 22 Dec 2011; revised 10 Feb 2012; accepted 26 Mar 2012; published 27 Mar 2012

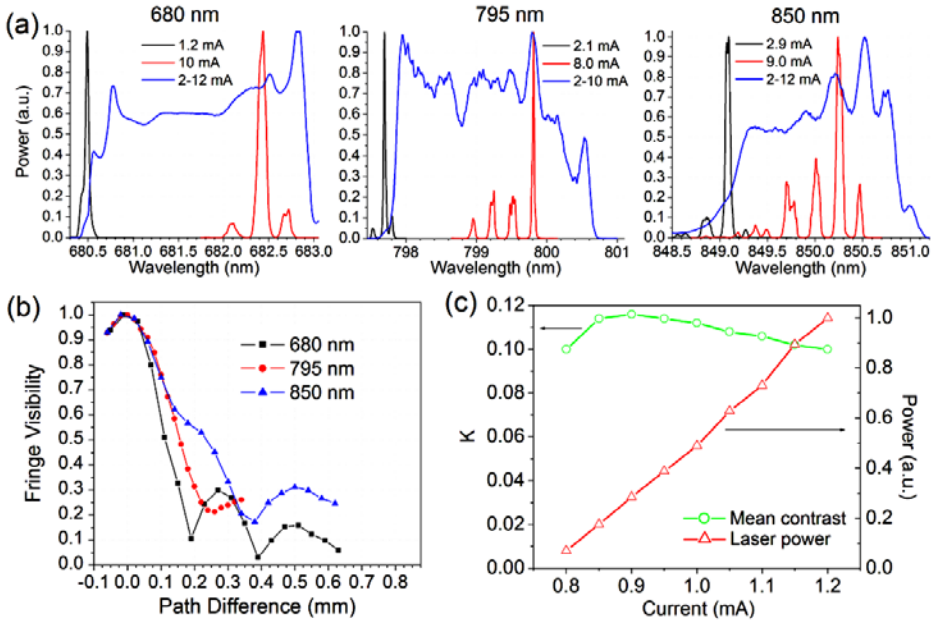

Fig. 1. (a) Spectra for 680 nm, 795 nm, and 850 nm VCSELs. In each case, measurements were taken at threshold current (black), peak power (red), and current sweep operation (SW) through a range optimized for each device. (b) Interferogram envelopes for three wavelengths in SW operation, showing similar coherence lengths in each case. (c) Speckle contrast for 680 nm VCSEL near threshold, showing high contrast dropping off as power is increased

between 40 and 60, depending on wavelength, giving a speckle reduction of approximately 85%. Table 1 gives a comparison of the estimated coherence lengths from spectral measurements and interferometry, with all three wavelengths.

Figure 1(c) shows VCSEL SM stability near threshold. Contrast ratios are obtained at M = 1 from an illuminated brain tissue phantom, composed of a silicone disc with embedded titanium dioxide particles. At 680 nm, the phantom's reduced scattering coefficient is 5.9 cm^{-1} and the absorption coefficient is negligible, similar to values found in rat cortex. As power is ramped up, speckle contrast first increases, and then begins to decrease as higher order transverse modes begin to appear. Within this current range, contrast is consistent within 15%, suitable level for obtaining LSCI images. This affords a range of powers covering an order of magnitude, within which we can consider emission to remain in single mode operation. This becomes important when trying to equalize image intensity between a number of VCSEL wavelengths, for each of which a detector may exhibit differing efficiency.

2.2. Imaging system

A schematic of our system is shown in Fig. 2. A 14-bit CCD camera (Rolera EM-C^2, QImaging, Surrey, British Columbia) is used to image the cortex illuminated by VCSEL devices. The system has been tested with wide-field imaging lenses producing magnifications of 1x to 4x. The maximum field of view is 1004 × 1002 pixels, each 8 × 8 μm. The CCD was chosen as a proof of concept image sensor for the VCSEL imaging technique, providing rapid imaging with high sensitivity and low noise. For a fully portable imaging system, a smaller imaging device such as a CMOS sensor would be required, and the authors are currently testing such a solution to complete the fully portable system, which will enable optical chronic neural imaging studies of freely behaving animals.

Calculated coherence lengths come from applying Eq. (4) to the measured spectra, and measured coherence lengths come from interferometry results. Values for $n_{speckle}$ are estimated

#160425 - $15.00 USD Received 22 Dec 2011; revised 10 Feb 2012; accepted 26 Mar 2012; published 27 Mar 2012

Table 1. Comparison of coherence lengths and resulting speckle pattern number for different VCSEL wavelengths

Wavelength (nm)	Spectral width (nm)	Power (mW)	l_c (calculated) (μm)	l_c (measured) (μm)	σ_s (mm)	n_s
680	2.3	2.5	90	110	5.6	50
795	2.4	1.3	120	150	8.9	60
850	1.6	2.6	230	220	8.9	40

based on measured coherence lengths. Average output powers are given for the sweep profiles described, and in each case represent roughly half of peak power.

The camera frame rate ranges from 34 frames per second (FPS) full-field, to >200 FPS for small ROIs. The data exhibited in this paper show experiments with 2x magnification of a 500 × 500 field of view, imaging a region of 2 × 2 mm. At this magnification, red blood cells are just resolvable and a wide field of view is possible. Higher magnifications can be used to see cells more clearly and focus on a smaller region. The CCD area selected allows the camera to run at 62 FPS. The CCD features EM gain capabilities, but for the purpose of linearity and accurate quantification of shot noise, this feature was not used. Camera exposure trigger readout is used to synchronize the VCSEL illumination with exposure frames. The three wavelength VCSEL devices are packaged as a single unit. Individual laser terminals are separated with a breakout box, and controlled with a fast switch (Keithley 7221) to turn on in sequence with received camera triggers. Programmable power sources (Keithley 6221) are used to drive the VCSELs. The 795 nm and 850 nm lasers share a power source (Source A), and are connected through the same switch card (Card 1), while the 680 nm laser is driven by a second source (Source B) and card (Card 2). The reason for this is the camera's higher sensitivity to 680 nm light; in this scheme, the 680 nm VCSEL can be pulsed for a shorter duration than the camera exposure, allowing all three wavelengths to make use of the camera's full dynamic range. Source A is driven in a sweep mode optimized for the higher wavelength VCSELs at 50 kHz. Source B is operated in a manually programmed wave form, which alternates between an optimized SW operation and DC current, SM operation. SM frames, as well as 795 and 850 SW frames, used 10-12 ms exposures, while 680 SW frames were pulsed for 3-4 msec. The trigger sequence used is illustrated in the lower right corner of Fig. 2(a), showing the exposure trigger as well as SW and SM waveforms. Other trigger sequences and waveforms are possible, including multi-wavelength LSCI, multi-exposure LSCI and rapid, two-wavelength IOSI.

2.3. Animal preparation

Animal preparation was completed according procedures outlined in our previous studies [15]. All animal studies were performed in accordance with ethics protocols approved by the University of Toronto Animal Care Committee. Male Sprague-Dawley rats, 150-250g, were used for imaging. Prior to surgical procedures, anaesthesia was induced using 5% isoflurane. During surgery and imaging, anaesthetic levels were reduced to 2-3%. Ischemia preparations were made through a single incision above the trachea. A single suture was tied loosely around the right common carotid artery, allowing for induction of partial ischemia [19]. The animal was then placed upright in a stereotaxic mount. Craniotomies approximately 4 mm in diameter were performed on the right hemisphere between bregma and lambda ridges, and the dura was removed. During ischemia imaging sessions, approximately one minute of baseline data was taken prior to induction.

Ischemia was induced by pulling the suture taut, occluding the artery. Ischemia was maintained for one minute before release, and reperfusion was imaged for three minutes following release.

#160425 - $15.00 USD Received 22 Dec 2011; revised 10 Feb 2012; accepted 26 Mar 2012; published 27 Mar 2012

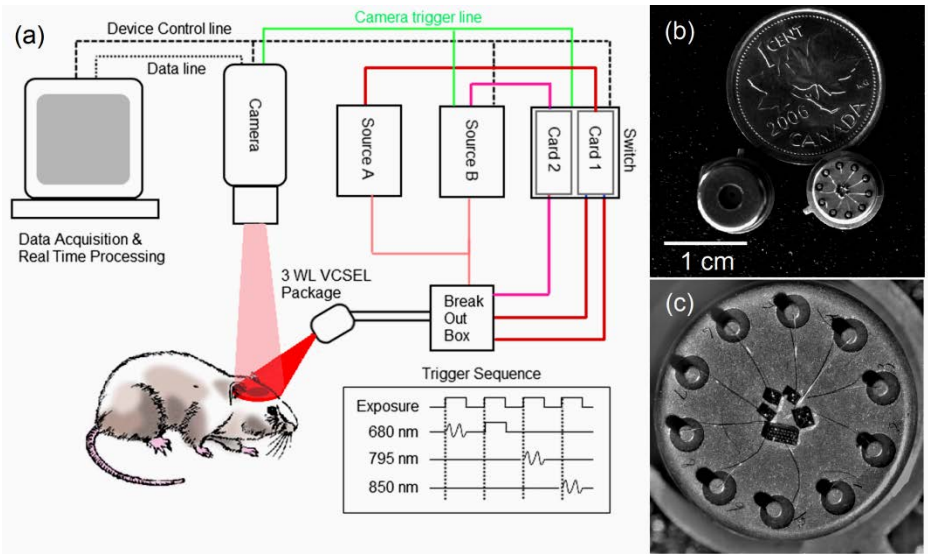

Fig. 2. (a) Multiwavelength system schematic. The three wavelength VCSEL package is driven using two current sources, which are alternated along with a rapid switch synchronized by a camera trigger. Software and hardware control is accomplished with a customized frame grabber program. The trigger sequence is shown on the bottom right, with SW and SM waveforms. (b) and (c) Detail of multi-wavelength VCSEL package. In the center of (c), three 850 nm wafers are visible, as well as one multi-VCSEL wafer each for 795 nm and 680 nm wavelengths.

2.4. Image analysis

Image processing was done in MATLAB and ImageJ. For laser speckle images, contrast maps were calculated from the standard deviation divided by the mean in 5x5 ROIs about each pixel. Noise correction algorithms were used to account for contrast contributions from camera read and shot noise. The read noise is treated as an additive constant which can be estimated from dark frame images, and the shot noise can be estimated as the square root of the mean number of electrons per pixel within each ROI, as measured in grey levels. By treating each contribution as an independent noise term, the corrected contrast can then be calculated as $K_c^2 = K_r^2 - \sigma_r^2 - \sigma_s^2$, where K_c is the corrected contrast, K_r is the raw contrast, and σ_r and σ_s are the estimated read and shot noise, respectively. A baseline LSCI map was established from the images collected before ischemic induction. During and after ischemia, relative flow speeds were calculated at each pixel based on the relative flow index, defined as $[K_0/K(t)]^2$, where K_0 is the baseline contrast and K(t) is the contrast at a later time [20].

Hemoglobin concentrations were calculated using a model based on a modified Beer Lambert law. Absorptions at three wavelengths are modeled by the system [14]:

$$\begin{bmatrix} \dfrac{\ln(R_{\lambda 1}(0)/R_{\lambda 1}(t))}{L_{\lambda 1}} \\ \dfrac{\ln(R_{\lambda 2}(0)/R_{\lambda 2}(t))}{L_{\lambda 2}} \\ \dfrac{\ln(R_{\lambda 3}(0)/R_{\lambda 3}(t))}{L_{\lambda 3}} \end{bmatrix} = \begin{bmatrix} \varepsilon_o^{\lambda 1} & \varepsilon_r^{\lambda 1} \\ \varepsilon_o^{\lambda 2} & \varepsilon_r^{\lambda 2} \\ \varepsilon_o^{\lambda 3} & \varepsilon_r^{\lambda 3} \end{bmatrix} \begin{bmatrix} \Delta[HbO](t) \\ \Delta[HbR](t) \end{bmatrix} \quad (5)$$

Here, R_λ represent the reflected intensities seen at the three wavelengths. ε_o and ε_r are the extinction coefficients of HbO and HbR at each wavelength respectively. Δ[HbO] and Δ[HbR] are the concentration changes of the two hemoglobin species. The parameters L_λ represent the

#160425 - $15.00 USD Received 22 Dec 2011; revised 10 Feb 2012; accepted 26 Mar 2012; published 27 Mar 2012

wavelength dependent path length factor in cortical tissue, which is the mean optical path length travelled through tissue before detection. These values are estimated using Monte Carlo simulation. The normal least squares equations are applied to fit an inversion of this model, solving for concentration changes based on the observed reflectance changes.

3. Results

In order to demonstrate the novel functionality of our imaging system, we analyzed high temporal resolution flow and oxygenation data in rodent cortical tissue. Several analysis methods were used to quantify changes as well as derive anatomical and functional information.

3.1. Cerebral ischemia dynamics

Results from a typical ischemia experiment are shown in Fig. 3. For the purpose of reproduction, the results shown here are compiled using five frame temporal averaging for IOSI, and 15 frame averaging for LSCI. With this method, IOSI and LSCI maps are produced three times a second. Without averaging, IOS and LSCI maps are produced 15 times a second. Figures 3(a)-(d) show images which qualitatively demonstrate the basic principles of LSCI and IOSI. Figure 3(a) is a baseline speckle contrast map. A large network of vessels of varying size is clearly visible. The contrast values seen here are somewhat lower than those found in fully developed speckle imaging, due to the relatively low f/# chosen for imaging, which causes reduced speckle size. We assert that, with the use of our noise correction algorithms as outlined in the methods section, the values observed here can be used to calculate flow speeds with similar accuracy as obtained from fully developed speckle. Figures 3(b)-(d) show maximum reflectance changes seen with 680 nm, 850 nm and 795 nm illumination, respectively. Changes are seen most strongly in a subset of the vessels highlighted in the LSCI map. Figures 3(e)-(h) show time series montages for maps of relative blood flow, Δ[HbR], Δ[HbO] and Δ[HbT], respectively. Images marked 0s indicate the onset of ischemia. We observe a clear dip in HbO as well as flow immediately after the onset of ischemia. A corresponding increase in HbR is seen at the same time, while total Hb exhibits a slight decrease. HbO and HbR changes are most substantial in a subset of larger vessels, as identified in the LSCI maps. These results are in accordance with similar previous studies [14]. The regions with heightened ischemic response are identified as veins. By comparing these vessels to the flow map calculated with LSCI, we can identify the remaining observed vessels as arteries. Regions with low flow and low oxygenation changes are identified as parenchyma or tissue containing unresolvable capillaries.

Based on the distinctions described above, time series plots were produced for ROIs within venous and arterial tissue. One large vein and one smaller vein, closer in diameter to the largest artery, are shown for comparison in Fig. 4. Each vascular component is seen to have a characteristic response during ischemia. Similar flow speed changes are seen in most vessels. Veins shown the greatest HbR and HbO changes, but the strength of the changes are strongly dependent on vessel diameter. HbT changes are similar between veins and arteries, but somewhat lower in the capillary tissue. After ischemia, partial reperfusion is seen as total Hb returns near baseline levels, but the individual components of HbO and HbR do not entirely recover on this time scale, and flow remains somewhat decreased. The noise seen in the LSCI plots come from variations due to respiratory and cardiovascular movement, as well as from statistical deviations in speckle values. The low recovery level of blood flow in particular can be ascribed to our ischemia model. When the knot of the carotid artery is released, vascular patency may not be fully recovered as some tension in the knot can remain. This will lead to a continued ischemic condition, and induce a vasodilative response in other vessels. The dilation of the vessels will allow HbT levels to recover, but flow values may remain reduced.

#160425 - $15.00 USD Received 22 Dec 2011; revised 10 Feb 2012; accepted 26 Mar 2012; published 27 Mar 2012

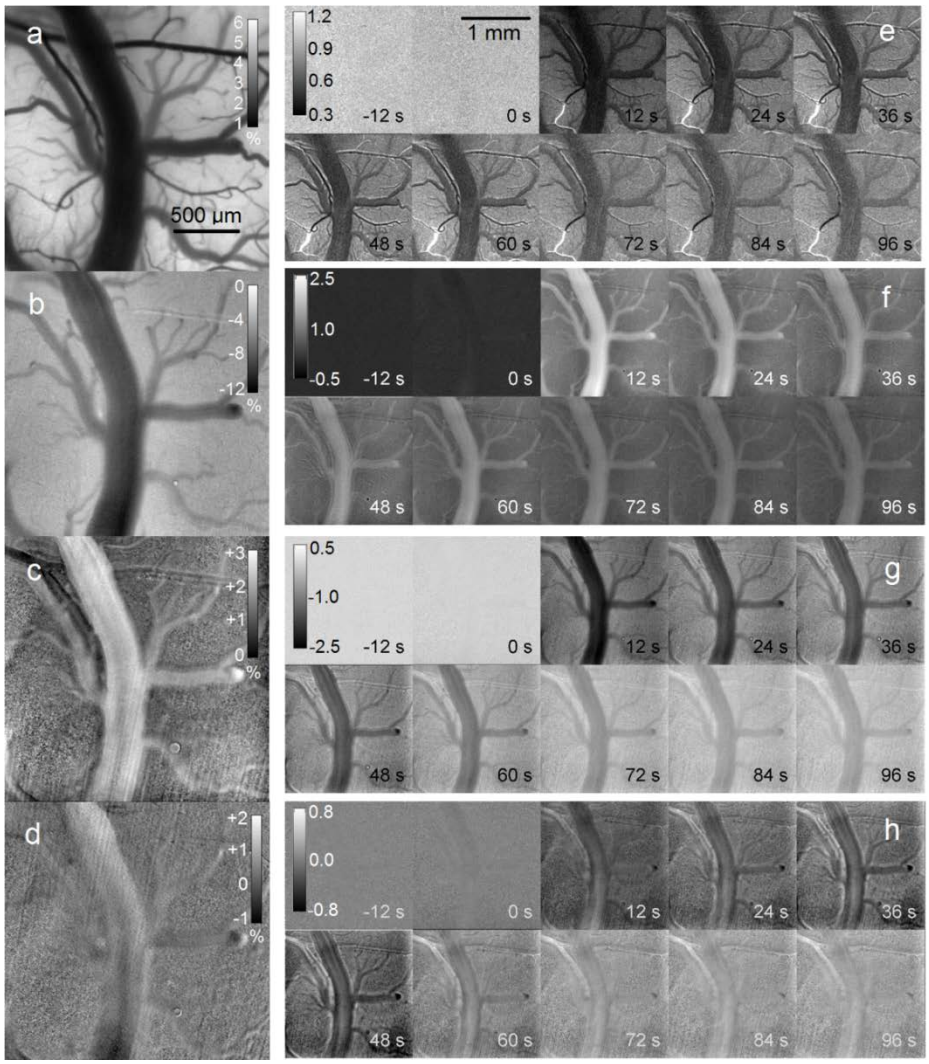

Fig. 3. Processed image maps of flow and oxygenation (see Media 1). (a) Baseline LSCI map, showing speckle contrast values. (b)-(d) Percentage change in reflectance at peak of ischemia, for 680, 850 and 795 nm illumination respectively. Scale is matched to (a). (e) Montage of changing flow values during ischemia using relative flow index. 0 s indicates onset of ischemia. (f)-(h) Montage of concentration changes during ischemia for HbR, HbO and HbT respectively. Units are 10^{-5} M. Scale is matched to (e).

These results indicate that our rapidly alternating VCSEL operation allows for very high quality, high temporal acquisition imaging of flow and oxygenation. The noise levels are sufficiently low to achieve sensitivity to micromolar concentration changes, and flow changes on the order of 10% or lower. The noise observed in IOSI is largely limited by shot noise, and further averaging can be used at this high acquisition rate to observe signal changes well below 0.1% at each wavelength. Signals at this level are commonly seen in sensori-motor stimulation studies [21,22].

3.2. Evaluating absolute flow velocities

LSCI itself cannot be used to establish flow direction and absolute speeds. Applying speckle imaging in tandem with more traditional erythrocyte tracking establishes directional flow velocities. Due to the low absorption of NIR light in blood, signal intensity differences seen

#160425 - $15.00 USD Received 22 Dec 2011; revised 10 Feb 2012; accepted 26 Mar 2012; published 27 Mar 2012

due to individual cells are quite low, making it difficult to easily track cells. Even in noisy data we have been able to implement cell tracking with line scans using spatiotemporal averaging. An outline of this procedure is shown in Figs. 5(a)-(c). To accomplish this, illumination at 680 nm in SW operation is used. Averaging of three individual lasers is used to further decrease speckle noise. A series of line scan maps are taken along the length of a vessel at different points on the diameter. The temporal progression along each line is plotted, producing in each case a position-time plot, as shown in Fig. 5(b). Spatial filtering is used to remove any horizontal or vertical line artifacts which may be present. A 2-D FFT is calculated for each line scan image and these are then averaged. The resulting FFT distribution, shown in Fig. 5(c) shows a strong component with either negative or positive slope, corresponding to forward and backward flow. The angle of this component can be used to calculate flow speed. The speeds obtained from a few vessels in this manner can be used to calibrate subsequent LSCI maps. If we apply a long exposure limit model, which predicts blood flow to be inversely proportional to speckle contrast squared, a single calibrated vessel can be used to estimate absolute flow velocities throughout the whole LSCI map [23]. Figure 5(d) shows the calibrated flow map as estimated using line scans on the vessels indicated in Fig. 5(a). Line scans were performed on a total of six vessels for verification of the estimate. A comparison between mean flow speeds established from line scans and from speckle for each vessel is shown in Fig. 5(e), where speckle flow index is defined as $1/K^2$, with K being the local speckle contrast. The mean and standard deviation values seen in the figure are taken within the same ROI for both speckle and line scans, using calculations from the speckle flow index and FFT angle respectively. The results show a strong correlation between speckle flow index and line scan velocity. Although direct quantification of errors has not been carried out for these studies, the model can be expected to remain quite accurate for a majority of vessels. Previous studies have shown that the long exposure limit is valid for a wide range of flow values [24,25]. For vessels with very low flow, such as vessel 4, the long exposure condition breaks down and speeds may be over-estimated. For very high flow, the noise limit of the camera combined with effects from static scatterers may result in under-estimation of speeds.

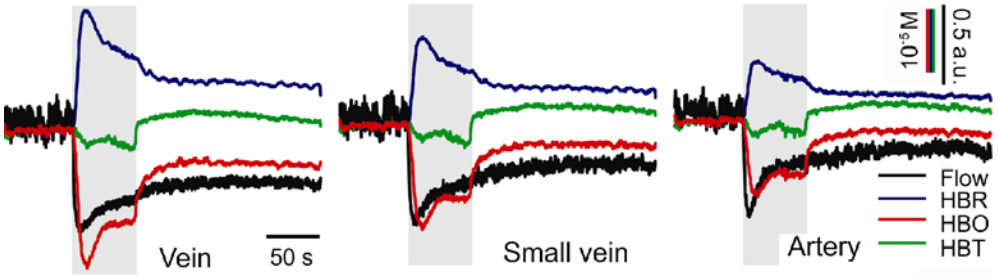

Fig. 4. Time course plots of 3 different vessels showing changes in blood flow, HbR, HbO and HbT. Grayed region indicates duration of ischemic induction. Significantly stronger ischemic responses are seen in veins compared to arteries. Further, larger veins exhibit stronger response than smaller veins.

With our imaging setup at 2x magnification, erythrocytes span approximately 1-2 pixels (~5-9 μm), and thus are quite difficult to resolve. In order to obtain a sufficient frame rate to track cells in vessels with speeds greater than ~4 mm/s, a reduced ROI is required. Rates of 110 FPS (or higher) can be achieved from a 200 × 200 ROI. Higher magnification can be used to facilitate this technique. The advantage of using this method for direction tracking, rather than velocity quantification, comes in our application to rapid imaging; we can determine flow direction by scanning a relatively small subset of vascular regions and extrapolating to connecting vessels. A direction map can then be produced for baseline flow, and the same data can be expected to remain unchanged during dynamic measurements. If a direction change did occur in a vessel, it would present itself first as a complete stopping of flow,

#160425 - $15.00 USD Received 22 Dec 2011; revised 10 Feb 2012; accepted 26 Mar 2012; published 27 Mar 2012

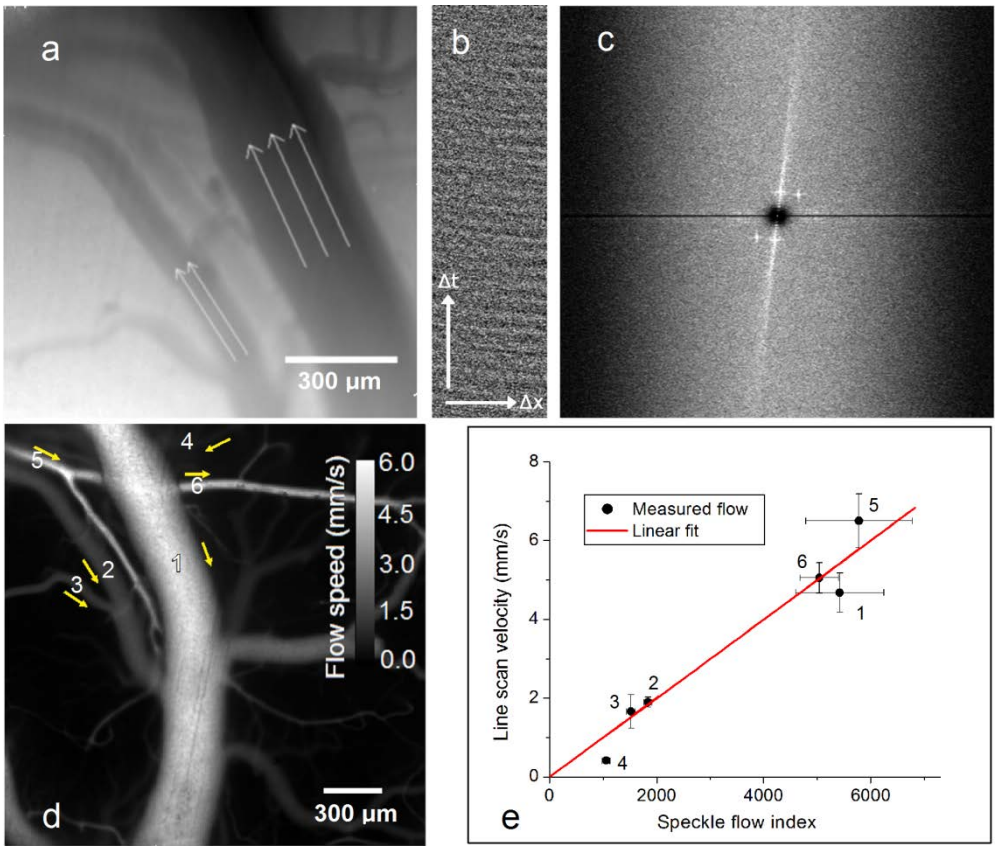

Fig. 5. Line scan averaging for flow quantification in noisy data. (a) Averaged raw image shows vessels as seen with 680 illumination. Selected vessel flow convention is indicated by arrows. (b) Single line scan 'carpet' shows pixel intensities over time. (c) FFT averaged over several carpets shows preferred components with slope proportional to flow speed (d) Estimated flow speed map, based on LSCI image and calibration from single vessel line scan. Yellow arrows indicate flow direction. (e) Correlation between speckle flow index and flow velocity established from line scan. Measurements on vessels 1-6 as indicated in (d) are shown.

before acceleration in the opposite direction. This type of anomalous behavior would be clearly seen from LSCI maps.

3.3. Principal component analysis of veins and arteries

The initial estimate of vein and artery classification based on oxygenation changes was largely qualitative, and could only be applied to the largest vessels. In order to distinguish smaller vessels with better accuracy, a more detailed method is necessary. Using the data garnered from combining flow and oxygenation measurements, we are able to apply statistical methods to classify veins and arteries. In order to accomplish this, the image was first segmented to create a mask of individual vessel branches. The data sets obtained from ischemia and baseline measurements were used to produce five quantities for each vessel compartment: mean HbO concentration change, mean HbR concentration change, mean relative flow speed change, mean baseline flow, and mean vessel diameter. Both veins and arteries can be expected to exhibit positive correlation between vessel diameter and baseline flow rate, but with different proportionality, therefore these two parameters were used as a primary discriminating factor. We expect arteries to exhibit generally higher flow. By further taking into account the changes measured during ischemia, greater accuracy in classification can be achieved. Oxygenation changes in particular are expected to be higher in veins, and this effect

#160425 - $15.00 USD Received 22 Dec 2011; revised 10 Feb 2012; accepted 26 Mar 2012; published 27 Mar 2012

can be used to enhance the separation between the two vessel populations. Before analysis, each quantity was normalized to its mean across all segments. Principal component analysis was performed on the resulting data to reduce dimensionality. The first principal component is interpreted to represent the large variability corresponding to vessel diameter, which sees similar variation in each type of vessel. The second component more closely indicates the differences between veins and arteries.

Figure 6 shows the result of the partition analysis. In Fig. 6 (a), two populations along different slopes are observed in the component 1-component 2 plane. Applying the reasoning described above, the two branches are identified as groupings of veins and arteries respectively. In order to separate the two groups according to slope, an iterative algorithm was used to perform two linear fits on an initially arbitrary partition. A bisection of the two fitted lines was used to produce a new partition criterion, and the fit was iterated on the new partitions until convergence was achieved. Figure 6 (b) shows the resulting partition when plotted against the three parameters of vessel diameter, HbO concentration and baseline flow speed. This plot more clearly shows the differences in flow and oxygenation which have allowed us to perform this classification. These observations are consistent with general understanding of neural hemodynamics and give confidence to our partition technique [26]. Figure 6 (c) shows the baseline flow map after vessel partitioning. The anatomical features observed further validate the partition. Vessel classifications are seen to be contiguous between branches, and the branching directions follow expected physiological conditions [27]: arteries predominantly branch towards the midline (the bottom of the image), while veins branch outwards.

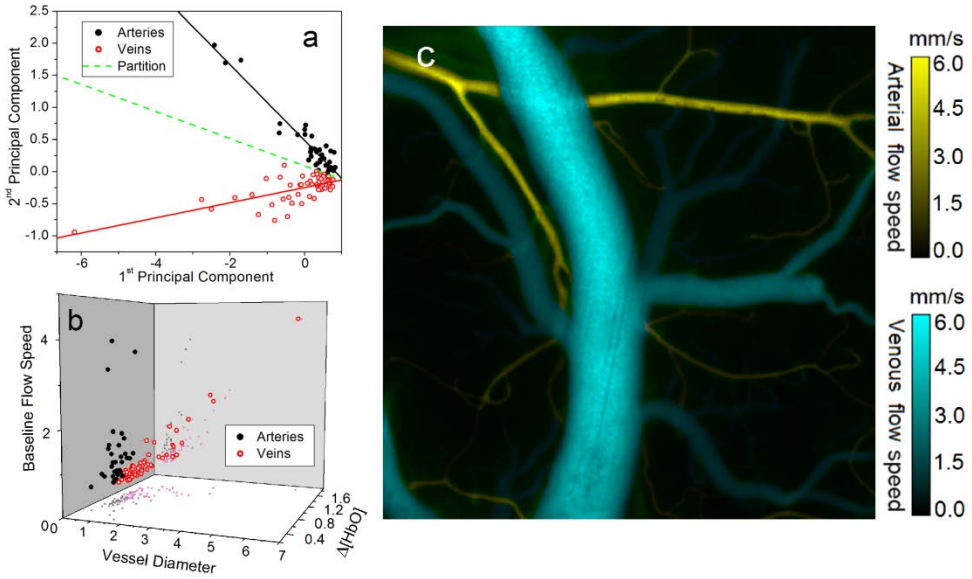

Fig. 6. Classification of veins and arteries using principal component analysis. (a) Scatter plot of data projections on first two principal components, showing partition estimate. The final result is found to be independent of initial partition. (b) 3D scatter plot showing vessel data against vessel diameter, baseline flow speed and [HbO] changes. All units are normalized. Projections in x-y and y-z are shown to aid visualization. (c) Resulting vessel classification mapped onto calibrated LSCI flow map. Yellow vessels are arteries and cyan vessels are veins.

4. Discussion

Our studies in this paper demonstrate a useful method for simultaneous imaging of cerebral blood flow and oxygenation using a compact light source. We have been able to track wide area dynamics rapidly, and assert that this technique can be applied to long-term monitoring.

#160425 - $15.00 USD Received 22 Dec 2011; revised 10 Feb 2012; accepted 26 Mar 2012; published 27 Mar 2012

VCSELs show unique potential in their application to portable imaging, due to their unique thermal properties. They can be used to produce coherent and incoherent illumination in a rapidly alternated scheme, allowing rapid dual modality imaging using a single, low power illumination source. While LEDs still generally provide lower noise than current swept VCSELs, in the scheme described here VCSEL noise can be brought within the shot noise limit, eliminating any apparent performance differences. A compact VCSEL source further allows for rapidly pulsed imaging that is not generally feasible with other laser sources. Considering the benefits discussed here, the use of VCSELs can lead to a system which is simplified in cost, power consumption and complexity, and presents an important step towards developing a portable imaging system. The imaging setup described here (Fig. 2) is reliant on CCD imaging, which is not amenable to miniaturization, resulting in the present non-portable imaging system for head-restrained animals. Recent work by our group towards a fully portable brain imaging solution involves testing portable CMOS sensors and designing the control electronics as well as optomechanical components for a portable imaging system. We see this method having important applications in the study of stroke progression and recovery, as well as in evaluation of drugs and treatment for brain and disease therapy. In particular, we see further development in miniaturizing this technique to produce a portable device. With portable and continuous monitoring of hemodynamics, we can gain a better understanding of stroke conditions such as periinfarct depolarizations (PIDs), and how they relate to flow changes in the ischemic penumbra [28,29]. Understanding the relation between flow and metabolization in the ischemic core and penumbra is a key factor in determining the mechanisms of cell death during stroke [30]. In epilepsy, flow and oxygenation information can be used to understand the temporal precedence of metabolic changes [4,31,32]. Our work demonstrates high temporal and spatial resolution and wide-field imaging, both of which are very important aspects of obtaining a full picture of neural activity. For future studies, we envision the addition of fluorescence imaging to improve the versatility of available techniques. Calcium sensitive dyes can be used to directly measure ions associated with neural activity in epilepsy. Alternatively, potassium sensitive dyes can be applied alongside LSCI to understand the effect of ion transfer or spatial buffering in glial cells during seizures [33–35]. Correct emission filter and laser wavelength selection is required to allow proper blocking of excitation wavelength, while passing the wavelengths needed for LSCI and IOSI.

The results we have shown indicate strong wide-field imaging performance when compared to other recent approaches. We use three rapidly pulsed wavelengths and capture images with a full frame rate of 60 FPS, in a 500 × 500 field of view. We have made use of dedicated imaging in a smaller field of view with rates faster than 100 FPS to calibrate blood flow velocity maps. We have been able to quantify micromolar hemoglobin concentration changes and image flow velocities ranging from approximately 1 to 10 mm/s. Recent work by another group on a head mounted fluorescent imaging system has demonstrated Ca^{2+} measurement alongside erythrocyte tracking at high spatial resolution [10]. This example provides similar temporal resolution to our system, using a single illumination source and narrow field imaging. However, our approach can be used to provide data in a wider field of view with somewhat lower resolution, and is still capable of tracking individual cells and evaluating full-field flow maps. Another recent example used multi-wavelength LED illumination to produce measurements of flow and oxygenation in a high speed, large scale setup [11]. This system showed very rapid imaging using microcontroller triggering of LED drivers. However, velocity measurements were only possible with magnified regions in a small field of view. We see our technique as a powerful alternative to these computationally intensive forms of imaging.

5. Conclusions

We have demonstrated a novel implementation of combined IOSI and LSCI measurement using VCSEL technology in multiple wavelengths. We have used our compact system for

#160425 - $15.00 USD Received 22 Dec 2011; revised 10 Feb 2012; accepted 26 Mar 2012; published 27 Mar 2012

monitoring of cerebral dynamics during artificial ischemic induction. The results we present show high sensitivity to reflectance changes while using laser sources for illumination. Rapidly switching between a highly coherent illumination scheme and a reduced coherence scheme allows us to simultaneously make measurements of oxygenation and blood flow *in vivo*. These values agree well with other recent studies of the same phenomena. Using coherent and incoherent illumination in a combined technique leads to several advantages: baseline flow values in a few vessels can be obtained using erythrocyte tracking with low noise SW illumination. This is used to calibrate later LSCI measurements within the long exposure limit. The combined data obtained using the two techniques simultaneously can be used to effectively classify veins and arteries in rodent cortex. Future work includes integration of miniaturized components for the purpose of developing portable monitoring of cortical hemodynamics. We see important applications in the study of stroke, epilepsy, and cancer.

Acknowledgments

The authors are grateful for the helpful discussions with James S. Harris, and Krishna V. Shenoy, Electrical Engineering, Stanford University, with Peter Carlen, Toronto Western Hospital, Toronto, and with Bojana Stefanovic, Sunnybrook Health Centre, Toronto. The authors also wish to thank Mary Hibbs-Brenner and Klein Johnson from Vixar, Inc. for assistance in epitaxial growth of VCSEL devices; to Joe Hayek from Toronto Western Hospital, for assistance with the ischemia model; to Mic Chaudoir from QImaging for helpful discussions and assistance in fast camera operations; to Breault Research Organization (BRO) for providing access to the ASAP software for academic purposes; and to Suzie Dufour and Yaaseen Atchia for assistance in data analysis for these studies. This work was supported in part through the University of Toronto departmental start-up funds to O. L., the Natural Sciences and Engineering Research Council of Canada (NSERC) Discovery Grant RGPIN-355623-08 and by the Networks of Centres of Excellence of Canada, Canadian Institute for Photonic Innovations (CIPI).

#160425 - $15.00 USD Received 22 Dec 2011; revised 10 Feb 2012; accepted 26 Mar 2012; published 27 Mar 2012